

Ambipolar Memristive Phenomenon in Large-Scale, Few-Layered αMoO_3 Recrystallized Films

Hyungsik Kim, Gwan-Hyoung Lee, James Hone, and Kenneth L. Shepard*

Studies of two-dimensional (2D) oxide materials are not common, primarily because of the difficulty in obtaining crystal sizes large enough to fabricate devices structures from exfoliation of bulk crystals. Among the layered oxide materials, alpha molybdenum trioxide (αMoO_3) is of particular interest because of its wide bandgap and high hole mobility. Here the growth of highly uniform, large-scale, ambipolar, few-layered αMoO_3 that is appropriate for nanofabrication is reported. Crystal grain sizes on the order of 5 μm are observed across samples as large as $10 \times 10 \text{ mm}^2$ with hexagonal grain boundaries and surface roughness of less than 500 pm rms. Exact [010] crystal orientation, characteristic of the layered atomic structure αMoO_3 , is observed. The measured bandgap energy is $\approx 2.8 \text{ eV}$. Carrier mobilities in polycrystalline films are $2.28 \text{ cm}^2 \text{ V}^{-1} \text{ s}^{-1}$ (hole) and $3.18 \text{ cm}^2 \text{ V}^{-1} \text{ s}^{-1}$ (electron) at room temperature in air. Simple field-effect device structures are characterized by ambipolar carrier transport producing memristive device characteristics, which is attributed to a polarization field produced by the strong coupling between electron and phonons in these crystals.

2D layered materials, such as graphene and transition-metal dichalcogenides (TMDs), have been of great research interest, and advances in large-area growth for many of these materials have enabled the fabrication of complex device structures.^[1–4] Progress in other 2D materials, in particular oxide 2D materials, has been more difficult because of challenges in obtaining large-area monolayers with sufficiently large grain sizes.^[5,6] Although there has been recent research on transition-metal-oxide materials, including titanium dioxide (TiO_2),^[7,8] gallium oxide (Ga_2O_3),^[9] and MoO_3 ,^[5] transition-metal-oxide layered materials have been rarely reported. MoO_3 , in particular, has drawn particular interest because of potential applications

in electrochromic devices,^[10–12] organic photovoltaic devices,^[13,14] organic light emission diodes,^[15,16] gas or chemical sensors,^[17] field effect transistors,^[5] and nanophotonic waveguides.^[18] More recently, there has been interest in using MoO_3 to control the carrier concentration of other 2D materials such as molybdenum disulfide (MoS_2) and tungsten diselenide (WSe_2)^[19] by the creation of surface dipoles.

For molybdenum oxide, each stoichiometry has very different chemical, electrical, and optical characteristics. αMoO_3 , one of many phases of molybdenum oxide, has very special electronic properties that make it of particular interest for electronic and optoelectronic devices. These include high electron mobility ($\approx 1100 \text{ cm}^2 \text{ V}^{-1} \text{ s}^{-1}$),^[5] a wide indirect bandgap ($\approx 3.3 \text{ eV}$),^[20] and high-relative dielectric constant ($\epsilon > 200$),^[5] making

it a good candidate to replace GaN in many applications. For high-voltage devices in particular, semiconductor materials are often characterized by Baliga's figure of merit (BFOM);^[21] $\mu\epsilon E_g^3$, where μ is mobility in unit of $\text{cm}^2 \text{ V}^{-1} \text{ s}^{-1}$, ϵ is dielectric constant in unitless, and E_g is bandgap energy in unit of eV. For αMoO_3 , BFOM can be as high as 363.7, compared to 24.6 for GaN and 1 for Si. Furthermore, the wide bandgap properties of αMoO_3 make possible optoelectronic devices in the ultraviolet by appropriate bandgap engineering. Adjusting oxygen and hydrogen intercalation allows bandgaps to be tuned in the range of 2.8–3.3 eV.^[20]

Although the crystal structure of αMoO_3 has been known for decades, synthesis of αMoO_3 through techniques such as atomic layer deposition,^[22] rapid thermal process,^[23] and oxidation of molybdenum metal^[24] have been largely unsuccessful because of poor control of growth conditions with a narrow band for stoichiometry, resulting in sparse αMoO_3 crystal flakes entangled with alternate lattice planes. Consequently, device results to-date have been from exfoliated crystals of molybdate, a natural ore.^[25]

Practical device fabrication requires the ability to synthesize highly uniform polycrystalline αMoO_3 in a manner similar to the chemical synthesis of other 2D materials such as CVD growth of graphene,^[26] MoS_2 ,^[27] and WS_2 .^[28] Here, we report for the first time large-scale growth of layered polycrystalline αMoO_3 using a thermal phase transition from amorphous MoO_3 which leads to high-quality crystallization. The resulting orthorhombic crystal structure in these films is verified and

Dr. H. Kim, Prof. K. L. Shepard
Department of Electrical Engineering
Columbia University
New York, NY 10027, USA
E-mail: shepard@ee.columbia.edu

Prof. G.-H. Lee
Department of Materials Science and Engineering
Yonsei University
Seoul 03722, South Korea

Prof. J. Hone
Department of Mechanical Engineering
Columbia University
New York, NY 10027, USA

 The ORCID identification number(s) for the author(s) of this article can be found under <https://doi.org/10.1002/admi.201801591>.

DOI: 10.1002/admi.201801591

characterized by scanning tunneling microscopy (STM), X-ray diffraction (XRD), X-ray photoelectron spectroscopy (XPS), and Raman spectroscopy. Atomic force microscopy (AFM) and Kelvin probe force microscopy (KPFM) are used to analyze surface properties, and Fourier-transform infrared (FT-IR) spectroscopy is used to analyze optical properties in the resulting layers. The electrical transport properties of the few-layer αMoO_3 crystals are also studied through the fabrication of simple field-effect transistors, demonstrating memristive characteristics of relevance to neuromorphic computing applications.^[29]

The crystal structure of MoO_3 has two phases, α and β . The β phase is metastable and has a monoclinic structure, while the α phase shows thermodynamic stability and an orthorhombic structure as shown in Figure S1a of the Supporting Information ($a = 3.962 \text{ \AA}$, $b = 13.855 \text{ \AA}$, $c = \text{Å}$, $\alpha = \beta = \gamma = 90^\circ$).^[5] In addition, α -phase material has a layered structure (with a layer thickness of $\approx 13.855 \text{ \AA}$) that is unique for this molybdenum oxide stoichiometry as shown in Figure S1b of the Supporting Information. Figure S1c of the Supporting Information shows the (010) plane of αMoO_3 , which defines the plane of the layers of the 2D crystal. Layered crystal growth is difficult to achieve of MoO_3 and is rarely reported. Oxygen vacancies commonly occur because αMoO_3 has corner connected or edge-shared MoO_6 octahedra in the unit cell as shown in Figure S1a of the Supporting Information, differing from the simple structure of TMDs, which requires MX_2 , where M is a transition metal atom (e.g., Mo, W) and X is a chalcogen atom (S, Se, or Te). Growth is further complicated by the narrow phase diagram for αMoO_3 .^[30]

In this work, we achieve single-crystal growth at high yield in a two-step process. First, thermal deposition below 80°C is used to grow a large-scale planar-uniform layer of amorphous molybdenum oxide with no discernible crystal structure. Deposition rates are kept below 0.01 nm s^{-1} to achieve dense films with a thickness range between 3 and 50 nm. Such thin films are required for efficient crystallization. As shown in Figure S2 of the Supporting Information, these thermally deposited amorphous MoO_3 films have a root-mean-square (rms) surface roughness of 0.3 and 0.6 nm rms for 3 nm and 50 nm thick layers, respectively. Following the deposition, these amorphous films are annealed in oxygen in a tube furnace to achieve crystallization, as shown in Figure S3 of the Supporting Information. Annealing times typically exceed 6 h (ramping up for 1 h, soaking for 5 h, and cooling naturally) at 350°C in an O_2 environment. The oxygen environment (99.999% purity) is essential to compensate for oxygen vacancies that would otherwise form in crystal formation. Any other gas environments (such as N_2 and Ar) result in inadequate crystal formation.

Figure 1a shows thermally deposited amorphous MoO_3 , patterned amorphous MoO_3 , annealed MoO_3 , and bright/dark field microscopy images for 30-nm-thick MoO_3 films. Generally, crystal orientation, grain boundary, and phase can be determined with electron backscatter diffraction (EBSD); however, in this case, the resolution of the EBSD detectors is too low to distinguish individual grains, which are clearly evident dark-field microscopy images. Figure 1a shows the comparison between bright-field and dark-field microscopy in 3 nm thick and 50 nm thick oxygen-annealed MoO_3 , showing clear grain-boundary contrast in each dark-field image that is not easily observed in

the corresponding bright-field image (Figure S4-1, Supporting Information). The surface morphology, thickness, crystal structure, and grain-boundary characteristics of these crystallized MoO_3 films are shown in Figure 1b–d. Crystallized, thick, amorphous MoO_3 (50 nm, Figure S4-1a,b, Supporting Information) show much clearer grain boundaries than those observed in thin amorphous MoO_3 (3 nm, Figure S4-1c,d, Supporting Information) when annealed under the same conditions. Surface morphology, as shown in Figure 1b, is very smooth and flat with 0.5 nm rms surface roughness and hexagonal crystals (Figure 1b; Figure S5, Supporting Information). Average grain size for films with thicknesses of 3 and 50 nm is 3.77 and 3.45 μm , respectively (see Supporting Information). From AFM analysis of multilayered crystals (Figure 1c), the thickness of one monolayer is $\approx 1.34 \text{ nm}$ ($b = 13.4 \text{ \AA}$), matching well theoretically estimated values and measured XRD data (Figure 2a).

To confirm crystal structure, STM was performed on the 3 nm thick recrystallized αMoO_3 sample. Figure 1d shows the resulting STM image, revealing clear atomic lattices ($a = 4.9 \text{ \AA}$, $c = 4.6 \text{ \AA}$, as shown in Figure S9-2, Supporting Information) across the observed area ($3.63 \text{ nm} \times 3.63 \text{ nm}$). Comparing with MoO_2 ($a = 5.610$, $b = 4.843$, $c = 5.526$, $\alpha = \gamma = 90^\circ$, $\beta = 119.62^\circ$),^[30] these lattice constants are larger than theoretically estimated values^[5] ($a = 3.962 \text{ \AA}$, $c = 3.699 \text{ \AA}$) for αMoO_3 . This would be the result of strain induced by lattice mismatch with the substrate or strain due to additional atoms in the lattice, such as adsorption of hydrogen atoms to the oxygen atoms.^[31] It is difficult to confirm the latter in the XPS analysis described below because the presence of interstitial hydrogen in the lattice will have little effect on the measured bond peaks. This distortion of the lattice constants also affects the bandgap. From STM (Figure S9, Supporting Information), we find a bandgap of $\approx 2.8 \text{ eV}$, which is within the theoretically estimated range^[31] and confirms the wide-bandgap nature of αMoO_3 monolayer films.

XRD measurement allows for the macroscopic conformational determination of lattice constants in the single-crystal films. Figure 2a shows the results of XRD analysis, which confirm the [010] orientation of the layered crystalline planes for both the 3 and 50 nm samples. The diffraction peaks in 2θ happen at exactly 12.8° , 25.8° , 39° excluding Si peaks at 33.22° , 61.92° (see Figure S6, Supporting Information). These peak positions nearly exactly match the [020], [040], and [060] direction in the orthorhombic crystal structure of αMoO_3 (ICDD card no. 35-0609, JCPDS reference card no. 5-0508). Intensity and broadening of the peaks in the XRD traces is affected by thickness variation in the films. The 3 nm thick αMoO_3 films showed smaller peak values in the same location as those observed on the 50 nm thick films, as shown the inset graph of Figure 2a. From this XRD measurement, lattice constants (a , b , c) can be extracted as $a = 3.9 \text{ \AA}$, $b = 13.8 \text{ \AA}$, $c = 3.9 \text{ \AA}$. Because of the size of the X-ray beam (an $\approx 6.35 \text{ mm}$ slit is employed), the lattice constants derived from XRD represent average values unlike the result from STM measurement.

The crystal stoichiometry was also analyzed by XPS, confirming that the samples have a Mo:O ratio of 1:3. As shown in Figure 2b, $\text{Mo}3/2_{3d}$ and $\text{Mo}5/2_{2d}$ binding energies are measured to be $233 \pm 0.3 \text{ eV}$ and $236 \pm 0.3 \text{ eV}$, respectively, further confirming the crystal stoichiometry (see Supporting Information). These doublets are unique to the spin-orbital

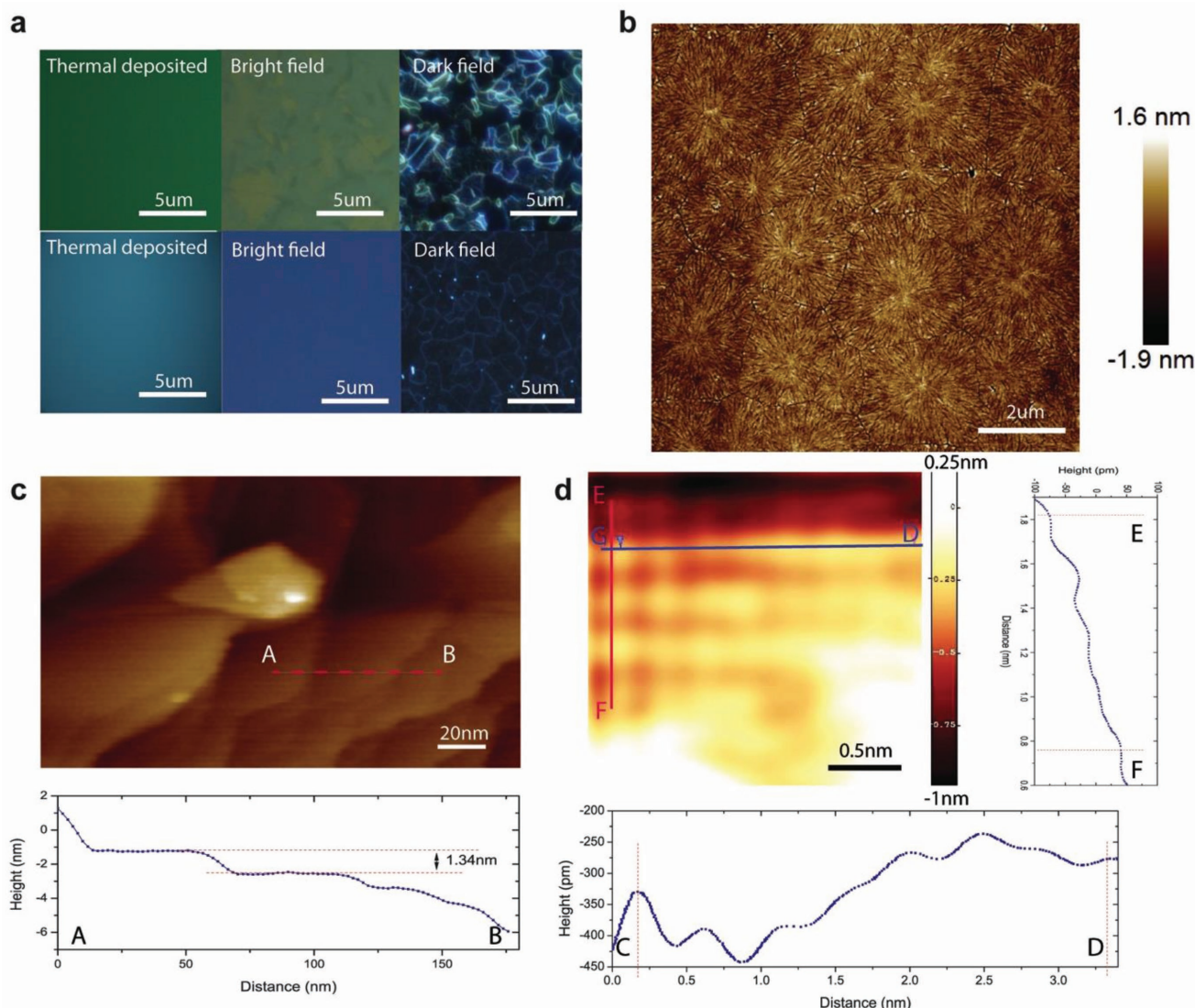


Figure 1. Microscope, AFM, and STM images of 3 nm thick α - MoO_3 . a) Thermally deposited amorphous MoO_3 , bright field and dark field images of annealed MoO_3 from the left. Top row images are for films ≈ 50 nm thick and the bottom row images are for films ≈ 3 nm thick. b) AFM images of 3 nm thick α - MoO_3 annealed in 350°C with O_2 environment. The measured surface roughness of 3 nm thick α - MoO_3 was 500 pm rms. c) Layered α - MoO_3 measured in AFM shows $b = 13.4$ Å. d) STM image of 3 nm thick α - MoO_3 shows $a = 4.9$ Å, $c = 4.6$ Å in the lattice structure. At this thickness, the films are approximately three layers thick.

coupling in MoO_3 (as distinct from what would be observed in MoO_2 , ≈ 229 eV for $\text{Mo}3/2_{3d}$ and ≈ 232 eV for $\text{Mo}5/2_{2d}$), confirming the 1:3 ratio of Mo and O.^[32,33] Figure 2c shows the observed Raman spectrum for our α - MoO_3 films, demonstrating well-defined chemical bonding of α - MoO_3 , consistent with previous studies.^[34] A micro-Raman map of the surface was formed from measurements in a 13×9 pixel array with $5 \mu\text{m}^2$ area per pixel (see Supporting Information). Raman spectroscopy of α - MoO_3 (symbols in Figure 2c are explained in Table S1, Supporting Information) reflects Mo–O and Mo=O bonds in the crystal, which have bending and stretching modes.^[5,33] The major peaks shown in Table S1 (Supporting Information) and Figure 2c, caused by oxygen vacancies, are a measure of the achieved crystalline uniformity (Figure S7, Supporting Information).^[5,33]

Defect bands in the samples were analyzed by FT-IR spectroscopy (Figure 2d). The peak positions and peak bandwidths in the IR spectra are influenced by crystal grain size, morphology, and defects.^[35] For wavenumbers less than 1020 cm^{-1} , atomic bonding structure determines the IR spectrum, and there is a one-to-one relationship between peaks found in the Raman spectrum with the minima found in the IR spectrum. The IR transmission of our sample shows one trench at 1160.7 cm^{-1} with a continuously increasing transmission at high wavenumbers. This is indicative of a defect band with the bandgap of α - MoO_3 located ≈ 0.14 eV below the conduction band edge, due to the polycrystalline nature of the sample.

We independently measured the work function of our α - MoO_3 films using KPFM (Figure S11, Supporting Information) and find this to be ≈ 5.1 eV in air, consistent with an

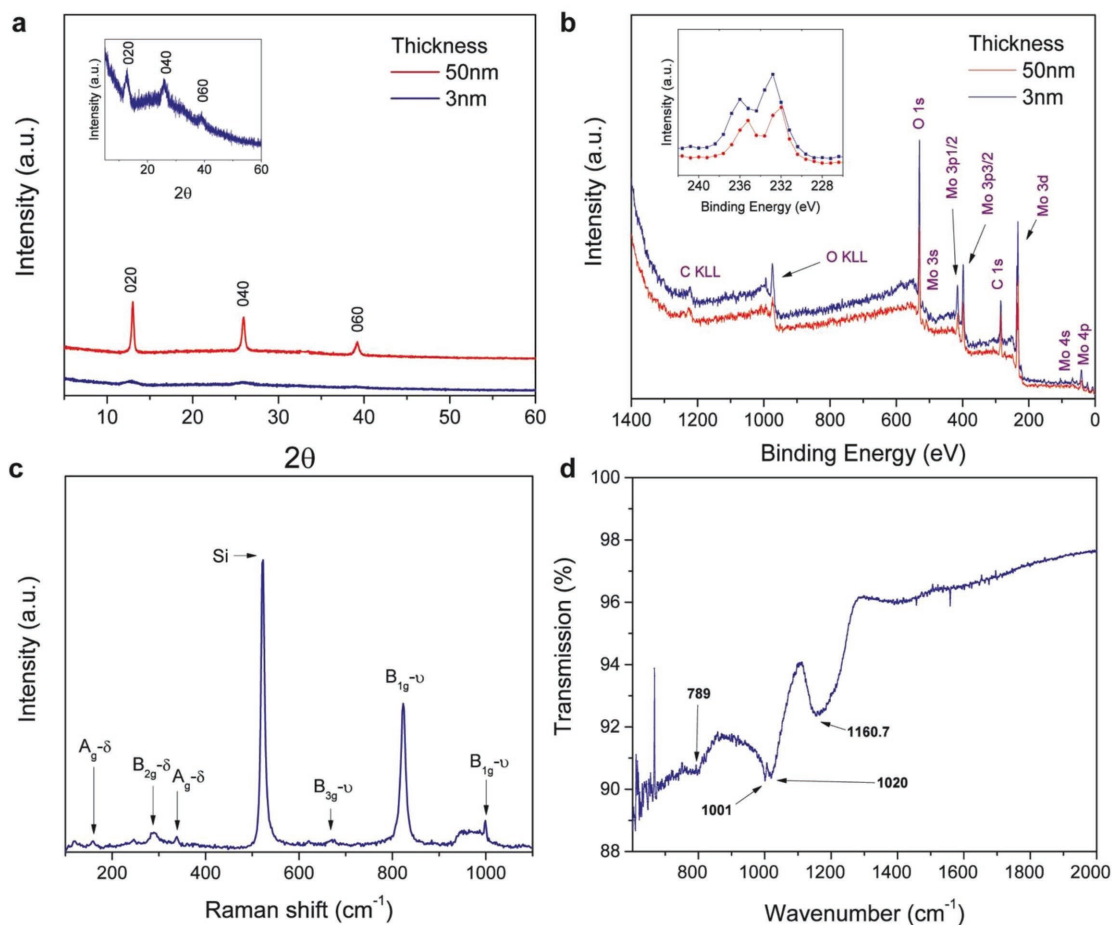


Figure 2. Crystal stoichiometry measured by a) XRD, b) XPS, c) Raman spectroscopy, and d) FT-IR spectroscopy for αMoO_3 films with thickness of 3 and 50 nm annealed at 350 °C in an O_2 environment. (a) XRD spectra depicts strong peaks in 13, 26, 38, corresponding [020], [040], [060], respectively. Inset graph shows diffraction pattern of 3 nm thick αMoO_3 . In the same positions with 50 nm thick αMoO_3 , [020], [040], and [060] peaks happened weak relatively because film thickness is thinner than 50 nm thick αMoO_3 . b) The ratio of molybdenum and oxygen can be determined in XPS spectra. (c) Raman spectrum in 3 nm thick αMoO_3 . Raman spectrum shows various bonding structure of αMoO_3 . The symbols in (c) are explained in Table S1 (Supporting Information). (d) FT-IR spectra of 3 nm thick αMoO_3 .

electron affinity of 6.7 eV, measured by ultraviolet photoemission spectroscopy and inverse photoemission spectroscopy in ultrahigh vacuum.^[36] These work functions make Ohmic contacts challenging due to high Schottky barrier heights. The surface potentials of transition metal oxides also significantly affect the ability to create good Ohmic contacts.

Despite these contact challenges, **Figure 3a** shows fabricated field-effect device structures. Few-layered αMoO_3 material (≈ 4.3 nm) is used as a channel layer between source and drain electrodes, which corresponds to approximately three layers. The substrate is a highly p-doped, (100)-oriented silicon wafer with a thermally grown layer of SiO_2 (900 nm) which functions as a backgate. We make source and drain contacts with deposition of Cr/Pd/Au (1 nm/30 nm/50 nm) on the surface of the αMoO_3 film. Cr in this case is used as an adhesion layer^[37] We estimate the contact resistance of the 1- μm -by-1- μm contacts in these devices to be ≈ 4.6 k Ω as shown in Figure S13b (see Supporting Information), which scales inversely with device width. Figure 3b,c shows representative current–voltage characteristics for these devices. αMoO_3 is generally considered

to be a p-type material. However, our device clearly shows ambipolar behavior in Figure 3b, characteristic of ab initio intrinsic doping with p-type characteristics at negative gate bias and n-type characteristics at positive gate bias. At the charge neutrality point in the curves of Figure 3b, we estimate the carrier concentration to be $\approx 7.6 \times 10^{10} \text{ cm}^{-2}$.

Amorphous MoO_3 is found to have a field effect mobility of only $\mu_{\text{eff}} = 1.4 \times 10^{-5} \text{ cm}^2 \text{ V}^{-1} \text{ s}^{-1}$ (Figure S12, Supporting Information). Crystallized αMoO_3 , however, is expected to have a bandgap between 2.8 and 3.3 eV and a mobility as high as $\mu_{\text{eff}} = 1100 \text{ cm}^2 \text{ V}^{-1} \text{ s}^{-1}$.^[5] Field-effect mobility in our devices can be calculated from $\mu_{\text{eff}} = \frac{L}{C_{\text{gate}} W V_{\text{ds}}} \frac{dI_d}{dV_{\text{gs}}}$, where $\frac{dI_d}{dV_{\text{gs}}}$ is the transconductance, I_d is the drain current, V_{gs} is the gate-to-source voltage, W is channel width, L is channel length, and C_{gate} is the gate capacitance. Our devices are formed in 4.3 nm films with approximately three layers, $W = L = 7 \mu\text{m}$, and $C_{\text{gate}} = 1.88 \times 10^{-15} \text{ F}$. As shown in Figure 3b, current–voltage (I – V) characteristics determine a field-effect mobility of $\mu_{\text{eff}} = 3.18 \text{ cm}^2 \text{ V}^{-1} \text{ s}^{-1}$ for holes (at $V_{\text{sd}} = 0.1 \text{ V}$) and

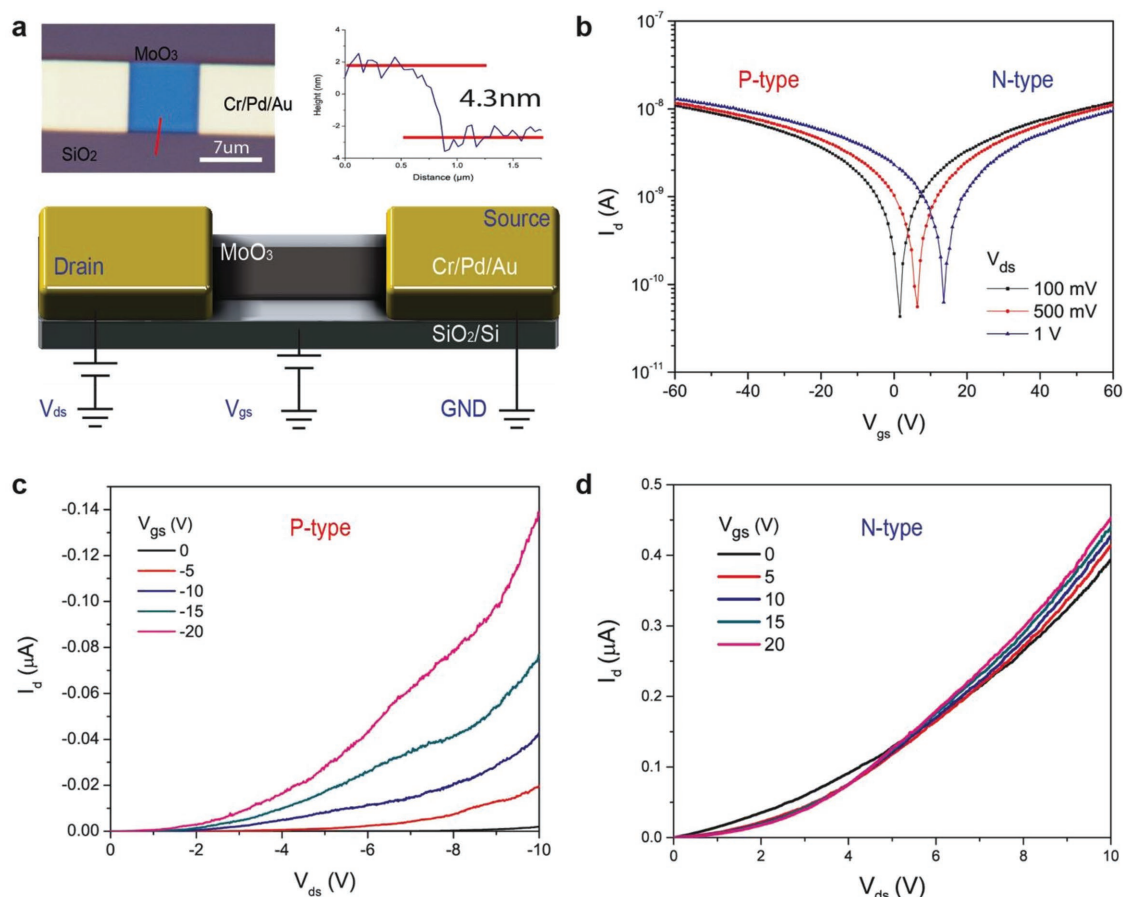


Figure 3. Electronic properties of 3 nm thick αMoO_3 annealed at 350 °C in an O_2 environment. a) Device structures. Inset: AFM measurement showing the channel thickness to be ≈ 4.3 nm. b) I_d as function of V_{gs} for three different values of V_{ds} , showing distinct ambipolar characteristics. The threshold voltage shifts from 1.6 to 13.6 V as V_{ds} is increased to 1 V. c) P-type behavior. V_{ds} swept uniformly in the direction from 0 to -10 V as V_{gs} is stepped from 0 to -20 V through the back gate. d) N-type behavior. V_{ds} is swept uniformly in the direction from 0 to 10 V as V_{gs} is stepped from 0 to 20 V through the back gate.

$\mu_{\text{eff}} = 2.28 \text{ cm}^2 \text{ V}^{-1} \text{ s}^{-1}$ for electrons (at $V_{ds} = 0.1$ V). Electron mobility is lower than previously reported values for single-crystal films because of the polycrystalline nature of our samples combined with the fact that the size of our devices exceeds our achieved grain size. The on/off ratio and subthreshold swing also vary with the biasing conditions and charge carrier type. The on/off ratio is $\approx 10^2$ while the subthreshold swing is ≈ 80 mV per decade for holes (at $V_{ds} = 0.1$ V) and ≈ 68 mV per decade for electrons (at $V_{ds} = 0.1$ V) (Figure 3b). For drain-to-source voltage magnitudes from 0 to ≈ 200 mV, the drain current (I_d), as shown in Figure 3c,d, shows the characteristics of thermionic transport due to the Schottky barrier contact at the source and the drain, which has a barrier height of ≈ 0.1 eV (consistent with the work function difference) and which varies with gate bias. As shown in Figure 3b, increasing V_{ds} shifts the threshold voltage in the positive direction, resulting in memristive behavior.

Further characterization of this memristive behavior, along with associated gate hysteresis, is shown in Figure 4a,b. Both phenomena are associated with charge-trapping by oxygen vacancies in αMoO_3 . In Figure 4a, gate hysteresis is observed with threshold voltage shifts as large as 5 V. The memristive

characteristics shown in Figure 4b are very similar to properties reported for TiO_2 and MoS_2 memristors.^[8,38] Figure 4b shows that the forward sweep of V_{ds} shows higher resistance and lower drain current than the backward sweep in the log-linear plot of I_d as a function of V_{ds} . The inset in Figure 4b provides a magnified scale for I_d as a function of V_{ds} for V_{ds} between 8 and 10 V and shows that the device has a transconductance that is typically less than $10 \mu\text{S } \mu\text{m}^{-1}$. Figure 4c,d shows the low-resistance and high-resistance states (LRS and HRS) at $V_{gs} = 0$ V in detail. The HRS switches to the LRS depending on the sweeping order and direction. The HRS corresponds to a resistance of $\approx 10^6 \Omega$ at 10 V with the LRS state about an order of magnitude lower.

Unlike the memristive properties in TiO_2 and MoS_2 , which depend on filamentary conductance paths, this memristive behavior can be attributed to polaronic scattering between ionic defects, produced by oxygen vacancies, and electrons, which are captured in the local potential of these ionic defects on the forward sweep. Production of polarons reduces the number of conducting holes in the valence band. This is matched with the shift of threshold voltages observed in Figure 4a, indicating the accumulation of holes in the channel. On the subsequent reverse sweep, holes can easily move with the help of

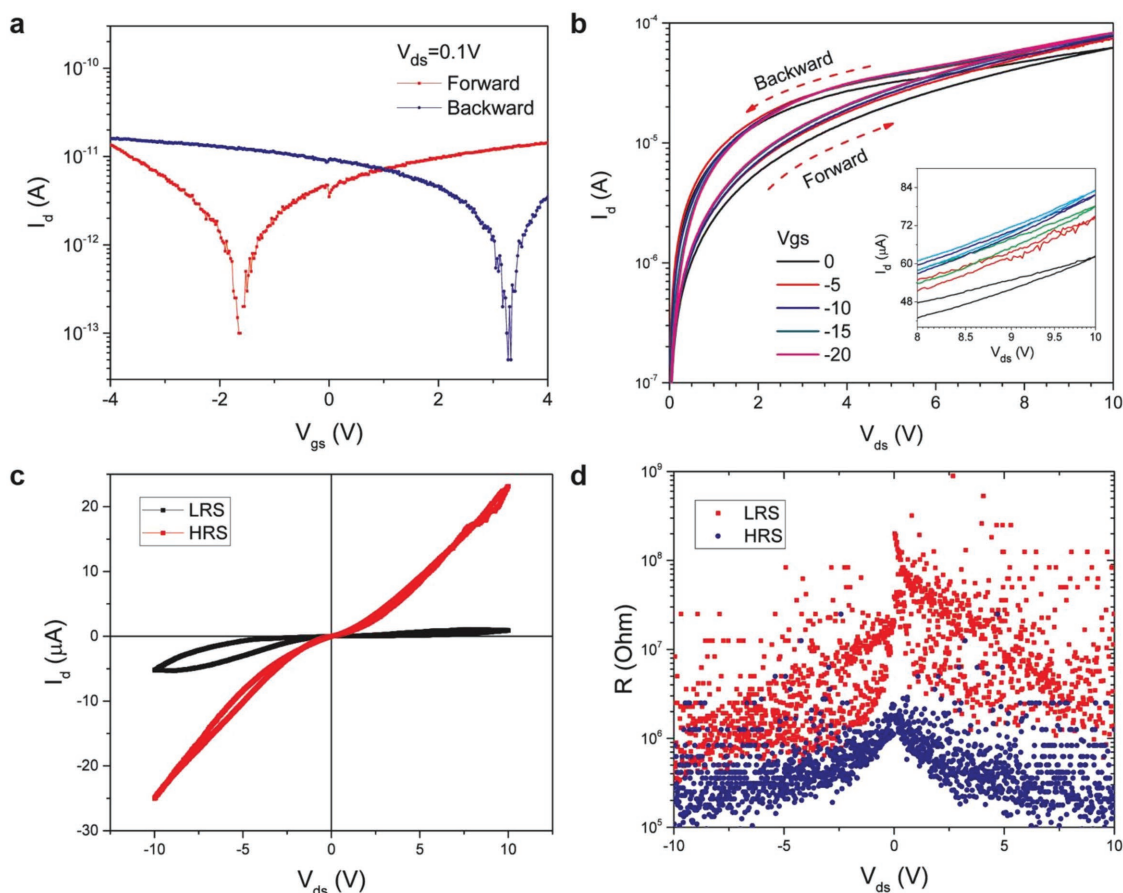


Figure 4. Strong hysteresis and memristive phenomenon of 3 nm thick αMoO_3 annealed in 350 °C with O_2 environment. a) Strong hysteresis. Transfer curve shows ambipolar characteristic as a function of V_{gs} in forward and reverse sweeps. The threshold voltage shifts from -1.65 V (forward) to 3.2 V (backward). b) Log-linear plot of I_{d} as a function of V_{ds} . Drain-to-source bias shows memristive phenomenon in forward and reverse V_{ds} bias sweeps. Inset: detail of I_{d} as a function of V_{ds} for V_{ds} between 8 and 10 V. c) Current characteristics of device having $W/L = 7/7$ μm in low-resistance and high-resistance states (LRS and HRS). d) Resistance difference in LRS and HRS at $V_{\text{gs}} = 0$ V (c,d).

these polarons, which locally increase the electric field, leading to larger electron current levels.^[39,40] These effects are immediately manifest in a differential in hole concentrations in the forward and backward sweeps as shown in Figure 4a, which shows a carrier concentration which is $3.71 \times 10^9 \text{ cm}^{-2}$ higher on the backward sweep.

High-voltage device characteristics of a device with a 30 nm SiO_2 gate dielectric and $W = L = 7$ μm are shown in Figure S14 of the Supporting Information with V_{ds} up to 60 V and gate biases chosen to produce n-type operation. This dielectric thickness is chosen only because it allows optical contrast to identify MoO_3 layers during fabrication. At a V_{gs} of 20 V, the triode region R_{on} is $\approx 1 \text{ M}\Omega$ (n-type operation), limited significantly by contact resistance. Device breakdown occurs at V_{ds} greater than 80 V due to thermal damage to the gate dielectric. Despite the wide bandgap of MoO_3 , improved contact resistance and gate dielectrics will be required to achieve competitive power devices from this material.

In summary, large-scale, uniform, few-layer αMoO_3 films were synthesized by recrystallization of amorphous MoO_3 film under carefully controlled phase-transition conditions. Ultrapure oxygen gas during the thermal phase transition prevents oxygen vacancies and helps deliver crystal sizes

in excess of 3 μm . The electrical properties of this material show ambipolar carrier transport and memristive behavior that can be explained by polaronic effect in the αMoO_3 lattice. Primarily because of contact resistance challenges, applications of this material for power electronics awaits further development.

Experimental Section

Crystal Growth: Molybdenum trioxide was deposited on a silicon oxide wafer by thermal evaporation. Source material (MoO_3 , CAS no. 1313-27-5, Catalog no. 203815) was purchased from Sigma-Aldrich. After deposition, the sample is annealed in a tube furnace (Lindberg M) with oxygen gas (Tech-Air, Inc., 99.999% purity). In crystal growth, the main experimental parameters are the annealing temperature and the pressure of the oxygen gas. Annealing temperatures were varied from 250 to 400 °C, and the gas flow was controlled by a common pressure regulator from 0 to 150 sccm. Good crystallinity was obtained at 350 °C and an oxygen flow rate of 50 sccm with a 1 h temperature ramp time, a 5 h anneal, and natural cool down (see Supporting Information).

Material Characterization: The surface morphology of molybdenum oxide was observed by optical and atomic force microscopy. Because

the bright-field images do not distinguish grain boundaries, dark-field imaging was primarily used to distinguish crystallization. Surface roughness and crystal growth were checked by AFM. When a crystal-like shape was confirmed in both tools, the crystal structure of samples was measured from XRD, Raman spectroscopy, and XPS. To measure crystal direction, XRD (Xpert3 Powder/Panalytical) was performed at 45 kV and 40 mV with a 30 s exposure. Atomic bonding structure in samples was observed through Raman spectroscopy (Renishaw, 532 nm laser, objective lens 100×). The stoichiometry of molybdenum oxide was analyzed by XPS (PHI5500, Mg, 15 kV 200W). STM was performed to confirm the orthorhombic structure of molybdenum trioxide. MoO₃ films were transferred onto a Au grid on a SiO₂/Si substrate for STM. The samples were degassed in the UHV measurement chamber at 200 °C for 12 h before measurements were performed. Finally, to measure work function, KPFM was used. The measurement was conducted in air with a Pt tip (Model number is PFQNE-AL) from Bruker, Co., and highly ordered pyrolytic graphite, Grade ZYB was used for reference (see Supporting Information).

Device Fabrication and Characterization: Recrystallized molybdenum trioxide is used as a channel layer to measure electronic properties. The fabrication procedure is depicted in Figure S10 of the Supporting Information. A lift-off method is used to pattern channel layer and electrodes. Poly(methyl methacrylate) (MicroChem PMMA A4 495 and A2 950) was coated in 2000 and 1000 rpm for 1 min on the sample. Following this, the sample was baked on hot plate at 180 °C for 2 min. For lithography, electron-beam lithography was used (Nano beam, nb4). To develop the pattern, IPA solution mixed with MIBK as 3:1 stored at −5 °C was used. Cr/Pd/Au of 1 nm/30 nm/50 nm were deposited as metal electrodes in the e-beam evaporator. After this, lift-off was done in acetone for 1 h. This lithography, deposition, and lift-off procedure was repeated for every layer. To measure electrical properties, a semiconductor parameter analyzer (Agilent B1500A) was used (see Supporting Information).

Supporting Information

Supporting Information is available from the Wiley Online Library or from the author.

Acknowledgements

This work was supported in part by the SRC/NRI INDEX Center. G.H.L. acknowledge support by Samsung Research Funding & Incubation Center of Samsung Electronics under Project No. SRFC-MA1502-12.

Conflict of Interest

The authors declare no conflict of interest.

Keywords

2D materials, ambipolar, memristor, molybdenum oxides

Received: October 11, 2018
Published online:

- [1] K. S. Novoselov, A. K. Geim, S. V. Morozov, D. Jiang, M. I. Katsnelson, I. V. Grigorieva, S. V. Dubonos, A. A. Firsov, *Nature* **2005**, 438, 197.
- [2] X. Cui, G.-H. Lee, Y. D. Kim, G. Arefe, P. Y. Huang, C.-H. Lee, D. A. Chenet, X. Zhang, L. Wang, F. Ye, F. Pizzocchero, B. S. Jessen, K. Watanabe, T. Taniguchi, D. A. Muller, T. Low, P. Kim, J. Hone, *Nat. Nanotechnol.* **2015**, 10, 534.

- [3] L. Li, Y. Yu, G. J. Ye, Q. Ge, X. Ou, H. Wu, D. Feng, X. H. Chen, Y. Zhang, *Nat. Nanotechnol.* **2014**, 9, 372.
- [4] L. Tao, E. Cinquanta, D. Chiappe, C. Grazianetti, M. Fanciulli, M. Dubey, A. Molle, D. Akinwande, *Nat. Nanotechnol.* **2015**, 10, 227.
- [5] S. Balendhran, J. Deng, J. Z. Ou, S. Walia, J. Scott, J. Tang, K. L. Wang, M. R. Field, S. Russo, S. Zhuiykov, M. S. Strano, N. Medhekar, S. Sriram, M. Bhaskaran, K. Kalantar-zadeh, *Adv. Mater.* **2013**, 25, 109.
- [6] S. Balendhran, S. Walia, H. Nili, J. Z. Ou, S. Zhuiykov, R. B. Kaner, S. Sriram, M. Bhaskaran, K. Kalantar-zadeh, *Adv. Funct. Mater.* **2013**, 23, 3952.
- [7] D. B. Strukov, G. S. Snider, D. R. Stewart, R. S. Williams, *Nature* **2008**, 453, 80.
- [8] J. J. Yang, J. P. Strachan, Q. Xia, D. A. A. Ohlberg, P. J. Kuekes, R. D. Kelley, W. F. Stickle, D. R. Stewart, G. Medeiros-Ribeiro, R. S. Williams, *Adv. Mater.* **2010**, 22, 4034.
- [9] M. Higashiwaki, K. Sasaki, T. Kamimura, M. Hoi Wong, D. Krishnamurthy, A. Kuramata, T. Masui, S. Yamakoshi, *Appl. Phys. Lett.* **2013**, 103, 123511.
- [10] C.-S. Hsu, C.-C. Chan, H.-T. Huang, C.-H. Peng, W.-C. Hsu, *Thin Solid Films* **2008**, 516, 4839.
- [11] J. N. Yao, K. Hashimoto, A. Fujishima, *Nature* **1992**, 355, 624.
- [12] M. Rouhani, J. Hobley, G. S. Subramanian, I. Y. Phang, Y. L. Foo, S. Gorelik, *Sol. Energy Mater. Sol. Cells* **2014**, 126, 26.
- [13] G. Wang, T. Jiu, P. Li, J. Li, C. Sun, F. Lu, J. Fang, *Sol. Energy Mater. Sol. Cells* **2014**, 120, 603.
- [14] H.-S. Kim, J. B. Cook, H. Lin, J. S. Ko, S. H. Tolbert, V. Ozoliņš, B. Dunn, *Nat. Mater.* **2017**, 16, 454.
- [15] J. Meyer, P. R. Kidambi, B. C. Bayer, C. Weijtens, A. Kuhn, A. Centeno, A. Pesquera, A. Zurutuza, J. Robertson, S. Hofmann, *Sci. Rep.* **2014**, 4, 1.
- [16] R. Liu, C. Xu, R. Biswas, J. Shinar, R. Shinar, *Appl. Phys. Lett.* **2011**, 99, 093305.
- [17] S. Balendhran, S. Walia, M. Alsaif, E. P. Nguyen, J. Z. Ou, S. Zhuiykov, S. Sriram, M. Bhaskaran, K. Kalantar-zadeh, *ACS Nano* **2013**, 7, 9753.
- [18] L. Zhang, G. Wu, F. Gu, H. Zeng, *Sci. Rep.* **2015**, 5, 17388.
- [19] C. Zhou, Y. Zhao, S. Raju, Y. Wang, Z. Lin, M. Chan, Y. Chai, *Adv. Funct. Mater.* **2016**, 26, 4223.
- [20] X. Sha, L. Chen, A. C. Cooper, G. P. Pez, H. Cheng, *J. Phys. Chem. C* **2009**, 113, 11399.
- [21] R. S. Pengelly, S. M. Wood, J. W. Milligan, S. T. Sheppard, W. L. Pribble, *IEEE Trans. Microwave Theory Tech.* **2012**, 60, 1764.
- [22] M. Diskus, O. Nilsen, H. Fjellvåg, *J. Mater. Chem.* **2010**, 21, 705.
- [23] O. Lupan, V. Cretu, M. Deng, D. Gedamu, I. Paulowicz, S. Kaps, Y. K. Mishra, O. Polonskyi, C. Zamponi, L. Kienle, V. Trofim, I. Tiginyanu, R. Adelung, *J. Phys. Chem. C* **2014**, 118, 15068.
- [24] S. Guimond, D. Göbke, J. M. Sturm, Y. Romanyshyn, H. Kühlenbeck, M. Cavalleri, H. J. Freund, *J. Phys. Chem. C* **2013**, 117, 8746.
- [25] R. L. Smith, G. S. Rohrer, *J. Solid State Chem.* **1996**, 124, 104.
- [26] X. Li, W. Cai, J. An, S. Kim, J. Nah, D. Yang, R. Piner, A. Velamakanni, I. Jung, E. Tutuc, S. K. Banerjee, L. Colombo, R. S. Ruoff, *Science* **2009**, 324, 1312.
- [27] A. M. van der Zande, *Nat. Mater.* **2013**, 12, 554.
- [28] Y. Gao, Z. Liu, D.-M. Sun, L. Huang, L.-P. Ma, L.-C. Yin, T. Ma, Z. Zhang, X.-L. Ma, L.-M. Peng, H.-M. Cheng, W. Ren, *Nat. Commun.* **2015**, 6, 1.
- [29] J. J. Yang, D. B. Strukov, D. R. Stewart, *Nat. Nanotechnol.* **2013**, 8, 13.
- [30] L. Chang, B. Phillips, *J. Am. Ceram. Soc.* **1969**, 52, 527.
- [31] P.-R. Huang, Y. He, C. Cao, Z.-H. Lu, *Sci. Rep.* **2015**, 4, 7131.

- [32] C. Julien, A. Khelifa, O. M. Hussain, G. A. Nazri, *J. Cryst. Growth* **1995**, 156, 235.
- [33] T. Brezesinski, J. Wang, S. H. Tolbert, B. Dunn, *Nat. Mater.* **2010**, 9, 146.
- [34] M. A. Camacho-López, L. Escobar-Alarcón, M. Picquart, R. Arroyo, G. Córdoba, E. Haro-Poniatowski, *Opt. Mater.* **2011**, 33, 480.
- [35] H. C. Zeng, *Inorg. Chem.* **1998**, 37, 1967.
- [36] J. Meyer, S. Hamwi, M. Kröger, W. Kowalsky, T. Riedl, A. Kahn, *Adv. Mater.* **2012**, 24, 5408.
- [37] L. Wang, I. Meric, P. Y. Huang, Q. Gao, Y. Gao, H. Tran, T. Taniguchi, K. Watanabe, L. M. Campos, D. A. Muller, J. Guo, P. Kim, J. Hone, K. L. Shepard, C. R. Dean, *Science* **2013**, 342, 614.
- [38] V. K. Sangwan, *Nat. Nanotechnol.* **2015**, 10, 403.
- [39] D. Emin, *Phys. Rev. B* **1993**, 48, 13691.
- [40] A. S. Alexandrov, P. E. Kornilovitch, *Phys. Rev. Lett.* **1999**, 82, 807.